Numerical study of enhanced mixing in pressure-driven flows in microchannels using a spatially periodic electric field

T. Krishnaveni, T. Renganathan, J. R. Picardo, and S. Pushpavanam*
Department of Chemical Engineering, IIT Madras, Chennai 600036, India
(Received 29 June 2017; revised manuscript received 24 August 2017; published 29 September 2017)

We propose an innovative mechanism for enhancing mixing in steady pressure driven flow of an electrolytic solution in a straight rectangular microchannel. A transverse electric field is used to generate an electroosmotic flow across the cross-section. The resulting flow field consists of a pair of helical vortices that transport fluid elements along the channel. We show, through numerical simulations, that chaotic advection may be induced by periodically varying the direction of the applied electric field along the channel length. This periodic electric field generates a longitudinally varying, three-dimensional steady flow, such that the streamlines in the first half of the repeating unit cell intersect those in the second half, when projected onto the cross-section. Mixing is qualitatively characterized by tracking passive particles and obtaining Poincaré maps. For quantification of the extent of mixing, Shannon entropy is calculated using particle advection of a binary mixture. The convection diffusion equation is also used to track the evolution of a scalar species and quantify the mixing efficiency as a function of the Péclet number.

DOI: 10.1103/PhysRevE.96.033117

I. INTRODUCTION

Lab-on-a-chip and other microfluidic devices play an important role in point of care medical diagnostics, chemical and biochemical analysis, and intensification of processes [1–4]. The flow in microchannels is typically steady, unidirectional, and laminar, with Reynolds numbers typically less than 100. Mixing here occurs solely due to molecular diffusion, which is a slow process, requiring large mixing times. Mixing can be enhanced by inducing secondary motion, which aids in mixing the fluid elements across the channel cross-section, i.e., in the direction transverse to the primary flow.

Micromixers are categorized into two classes: passive mixers and active mixers. Passive mixers utilize the energy from the primary flow to drive secondary flows, whereas active mixers require an external energy input to mix the fluids. Different types of mixers studied in the past include the staggered herringbone mixer [5], the serpentine mixer which uses Dean vortices [6], electroosmotic mixers [7], etc. Nguyen and Wu [8] and Lee *et al.* [9] have comprehensively reviewed the different types of passive and active mixers. Active mixers typically lead to more intense and controllable mixing. In electroosmotic mixers, active mixing is induced by using an electric field. The primary advantages of electroosmotic driven mixers are that it does not involve any moving parts nor does it require any geometrical modifications to the channel.

Electro-osmosis is based on the surface charge of the microchannel. The walls of a channel typically acquire a surface charge when they come in contact with an electrolytic solution [10]. When the electrolytic solution flows through such a channel, the counter ions in the solution accumulate near the charged walls, forming an electrical double layer (EDL). When an external electric field is applied tangential to the channel wall, the fluid in the EDL experiences a body force equal to the charge density multiplied by the electric field strength. This causes the fluid near the wall to move along or opposite to the direction of the electric field. The momentum from this thin EDL is transmitted into the bulk fluid by viscous stresses resulting in an electroosmotic flow (EOF). Several studies on the use of electro-osmosis to transport fluids in micro-channels exist in the literature [11–13].

Chaotic advection in a flow field refers to the chaotic behavior of Lagrangian trajectories of passive tracer particles that are advected by the flow [14]. Chaotic advection can exist when the flow is laminar, and therefore it has been extensively utilized to enhance mixing in micro-devices, in which the Reynolds number is very small [15]. In two-dimensional (2D) flows, chaotic advection can occur only if the flow is time-dependent. Typical devices employ a periodic (in time) 2D flow field in which streamlines of the first half cycle intersect with streamlines of the second half cycle. Many two-dimensional EOF mixers have been studied, and the effects of various unsteady flow fields and complex surface potential distributions have been analyzed [16–19].

Chaotic mixing can also be generated in three-dimensional *steady* flows, provided that the flow field varies along the streamwise direction [15]. The trajectories of passive tracers are then chaotic along the streamwise direction, in addition to being chaotic in time. The basic idea is to generate overlapping secondary vortex patterns that alternate periodically along the stream-wise direction. This idea was first introduced by Jones *et al.* [20], who used centrifugally driven Dean vortices to generate chaotic mixing in a twisted curved channel mixer. Many of the mixers that have since been proposed are based on curved geometries, in which streamline overlapping is induced by modifying the channel geometry [15] or the surface properties of the walls [21]. An example of a mixer that does not use curved sections is the staggered herringbone mixer [5]. A common feature of all these passive mixers is that the intensity of mixing is dependent on the strength of the primary axial flow.

There are relatively few studies on mixers using three-dimensional steady EOF. Pacheco *et al.* [22] and Kim *et al.* [23]

*spush@iitm.ac.in

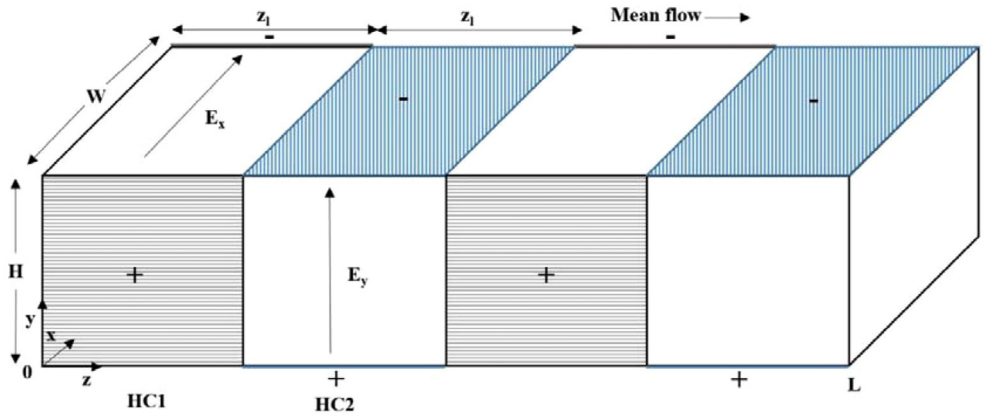

FIG. 1. Schematic of the electroosmotic mixer with a rectangular cross-section sustaining a pressure driven axial flow with an applied electric field which alternates in direction. Electrodes placed on the left and right walls impose a horizontally directed electric field in the first half cell (HC1) and electrodes place on top and bottom walls impose a vertically directed electric field in the second half cell (HC2). Two unit cells are shown.

simulated mixing in a microchannel in which both the axial and transverse flows are generated by electroosmosis. Lynn *et al.* [24] proposed a micromixer that has a pressure-driven primary axial flow, along with secondary flows that are induced electro-osmotically by incorporating electrodes underneath the channel. The secondary flow was varied along the length of the channel to enhance mixing, by adjusting the width between the electrodes.

The various mixers that have been analysed in the literature have certain limitations. These include the need for unsteady flows, complex surface potential distribution, and the inability to control mixing independently of the flow rate. In this theoretical work, we propose a mixer which can overcome these shortcomings. We show that chaotic mixing can be achieved in steady flow through a straight microchannel, with uniform surface potential distribution, by applying a longitudinally varying electric field. The flow of an electrolyte solution in a straight rectangular microchannel is considered. The primary axial flow is pressure driven. Transverse flow is induced electroosmotically by applying an electric field in a direction transverse to the primary flow. The orientation of the transverse field is varied periodically along the length of the channel. This results in a steady three-dimensional flow, with a transverse component that varies periodically along the streamwise direction, such that the projected streamlines of the secondary flow in each half-cell overlap. As discussed above, this is a classic recipe for inducing chaotic mixing in three-dimensional steady channel flow. This electroosmosis based chaotic mixer has advantages of efficient and controllable mixing at low flow rates and small channel dimensions. The electric field provides a handle to control mixing in the system, which is independent of the flow rate prevailing in the channel.

This paper is organized as follows: In Sec. II, the geometry of the proposed electroosmotic mixer is described. The mathematical model for the velocity field is discussed in Sec. III. The important features of the velocity field are described in Sec. IV. We characterize mixing using different approaches—Poincaré sections, Shannon entropy, and mixing index based on the transport of a diffusing scalar—in Sec. V. The major conclusions are summarized in Sec. VI.

II. GEOMETRY OF ELECTROOSMOTIC MIXER

The electroosmotic mixer being analyzed consists of a straight microchannel with a rectangular cross section of width "W" and height "H" as shown in Fig. 1. The fluid flows along z direction from $z = 0$ to $z = L$. Surface charge (a negative charge for glass microchannels) is assumed to be uniform at the microchannel walls. Mixing is induced in this microchannel by applying a DC electric field whose direction varies periodically in two perpendicular directions as depicted in Fig. 1. For the purpose of the analysis the microchannel is divided into unit cells. Each unit cell contains two half cells, each of length "z_l." In the first half cell (HC1), the electric field is applied horizontally (along x direction) by placing electrodes along the left and right walls of the channel as viewed from the end of the microchannel. In the second half cell (HC2), the electric field is applied vertically (along y direction) by placing electrodes along the top and bottom walls of the channel. These two half cells constitute the unit cell of length $2z_l$. This alternating pattern is repeated periodically as shown in Fig. 1

III. MODEL DEVELOPMENT

In this work, the model to describe the flow field is developed based on the following assumptions:

(1) Fluid flow is steady, laminar and fully developed in each half cell, and there is no transition region between the two half cells.

(2) Gravitational force is negligible.

(3) The fluid flowing is Newtonian.

(4) The zeta potential is uniform along the channel length.

(5) The fluid properties are independent of ion concentration and the local applied electric field strength.

(6) Joule heating effect from the applied electric field is negligible and the system is isothermal.

(7) Streaming potential induced by the fluid flow is negligible.

The fluid flow in the microchannel is pressure driven. In the creeping flow limit, the flow of an incompressible Newtonian

fluid in the presence of an electric field is governed by

$$-\vec{\nabla}P + \mu\nabla^2\vec{u} + \vec{E}\rho_e = 0. \quad (1)$$

Here P is the pressure, $\vec{u}$ is the velocity field (u,v,w), $\vec{E}$ $(E_x,E_y,0)$ is the applied electric field, ρ_e is the net charge density, and μ is the viscosity of the solution. In the above equation, the effect of electric field manifests as a body force.

The net charge density is related to the electric potential (Φ) by the equilibrium Boltzmann distribution. For a symmetric electrolytic solution, this is given by

$$\rho_e = -2nen_\infty \sinh\left(\frac{ne\Phi}{k_bT}\right). \quad (2)$$

Here k_b is the Boltzmann constant, T is the absolute temperature of the solution, e is the charge of a proton, n_∞ is the bulk ionic concentration, and n is the valence of the ions. According to the theory of electrostatics, the distribution of electric potential (Φ) is governed by the Poisson equation [10],

$$\nabla^2\Phi = \frac{-\rho_e}{\varepsilon_r\varepsilon_0}, \quad (3)$$

where ε_0 is the permittivity of vacuum and ε_r is the dielectric constant of the solution. Substituting Eq. (2) for the net charge density in Eq. (3) results in the Poisson-Boltzmann equation,

$$\nabla^2\Phi = \frac{2nen_\infty}{\varepsilon_r\varepsilon_0}\sinh\left(\frac{ne\Phi}{k_bT}\right), \quad (4)$$

This is nondimensionalized using the following characteristic scales:

$$x_{ch} = W, \quad y_{ch} = W, \quad \Phi_{ch} = \frac{k_bT}{ne}. \quad (5)$$

The dimensionless variables and groups that arise are

$$\bar{x} = \frac{x}{x_{ch}}, \quad \bar{y} = \frac{y}{y_{ch}}, \quad \bar{\Phi} = \frac{\Phi}{\Phi_{ch}}, \quad \lambda = \frac{H}{W}. \quad (6)$$

Equation (4) expressed in dimensionless form is

$$\frac{\partial^2\bar{\Phi}}{\partial\bar{x}^2} + \frac{\partial^2\bar{\Phi}}{\partial\bar{y}^2} = K^2\sinh(\bar{\Phi}). \quad (7)$$

In Eq. (7), $K^2 = (kx_{ch})^2$ is the Debye-Huckel parameter, where $k^2 = 2n^2e^2n_\infty/\varepsilon_r\varepsilon_0k_bT$. Here $1/k$ is a length scale representative of the thickness of the EDL.

This is subject to the boundary conditions

$$\begin{aligned}
\bar{\Phi}(\bar{x}=0) &= \bar{\zeta} \quad 0<\bar{y}<\lambda,\\
\bar{\Phi}(\bar{x}=1) &= \bar{\zeta} \quad 0<\bar{y}<\lambda,\\
\bar{\Phi}(\bar{y}=0) &= \bar{\zeta} \quad 0<\bar{x}<1,\\
\bar{\Phi}(\bar{y}=\lambda) &= \bar{\zeta} \quad 0<\bar{x}<1.
\end{aligned} \quad (8)$$

In Eq. (8), $\bar{\zeta}$ is the dimensionless ζ potential defined in terms of the ζ potential at the solid/liquid interface ζ, i.e., $\bar{\zeta} = ne\zeta/k_bT$.

Equation (1) is nondimensionalized and the dimensionless velocity field is governed by

$$\frac{\partial\bar{u}}{\partial\bar{x}} + \frac{\partial\bar{v}}{\partial\bar{y}} = 0, \quad (9)$$

$$\frac{\partial^2\bar{u}}{\partial\bar{x}^2} + \frac{\partial^2\bar{u}}{\partial\bar{y}^2} - \frac{\partial\bar{P}}{\partial\bar{x}} + G_x\bar{\rho}_e = 0, \quad (10)$$

$$\frac{\partial^2\bar{v}}{\partial\bar{x}^2} + \frac{\partial^2\bar{v}}{\partial\bar{y}^2} - \frac{\partial\bar{P}}{\partial\bar{y}} + G_y\bar{\rho}_e = 0, \quad (11)$$

$$\frac{\partial^2\bar{w}}{\partial\bar{x}^2} + \frac{\partial^2\bar{w}}{\partial\bar{y}^2} = -1, \quad (12)$$

subject to the following boundary conditions:

$$\begin{aligned}
\{\bar{u},\bar{v},\bar{w}\} &= 0 \quad \text{at} \quad \bar{x}=0 \quad \text{for} \quad 0<\bar{y}<\lambda,\\
\{\bar{u},\bar{v},\bar{w}\} &= 0 \quad \text{at} \quad \bar{x}=1 \quad \text{for} \quad 0<\bar{y}<\lambda,\\
\{\bar{u},\bar{v},\bar{w}\} &= 0 \quad \text{at} \quad \bar{y}=0 \quad \text{for} \quad 0<\bar{x}<1,\\
\{\bar{u},\bar{v},\bar{w}\} &= 0 \quad \text{at} \quad \bar{y}=\lambda \quad \text{for} \quad 0<\bar{x}<1.
\end{aligned} \quad (13)$$

In the above equations, $\bar{u},\bar{v},\bar{w}$ are dimensionless velocities along the x,y,z directions, respectively, $\bar{P}$ is the dimensionless pressure, $\bar{E}_x$ and $\bar{E}_y$ are the dimensionless applied electric fields in the x and y directions, respectively. These are nondimensionalized using the characteristic scales:

$$\begin{aligned}
z_{ch} &= x_{ch}, \quad P_{ch} = -\frac{dp}{dz}x_{ch}, \quad U_{ch} = \frac{P_{ch}{x_{ch}}^2}{\mu},\\
E_{ch} &= \frac{|\zeta|}{x_{ch}}, \quad \rho_{e_{ch}} = 2nen_\infty.
\end{aligned} \quad (14)$$

This results in the following dimensionless variables and dimensionless groups:

$$\begin{aligned}
\bar{P} &= \frac{P}{P_{ch}}, \quad \{\bar{u},\bar{v},\bar{w}\} = \frac{\{u,v,w\}}{U_{ch}}, \quad \bar{\rho}_e = \frac{\rho_e}{\rho_{e_{ch}}},\\
\{\bar{E}_x,\bar{E}_y\} &= \frac{\{E_x,E_y\}}{E_{ch}}; \quad G_x = \frac{E_{ch}\rho_{e_{ch}}x_{ch}\bar{E}_x}{\mu U_{ch}},\\
G_y &= \frac{E_{ch}\rho_{e_{ch}}x_{ch}\bar{E}_y}{\mu U_{ch}}, \quad \bar{z}_l = \frac{z_l}{z_{ch}}.
\end{aligned} \quad (15)$$

The formal derivation of the governing equations is given in the Appendix. These equations can be viewed as the zeroth-order solution of a perturbation series expansion of the full Navier Stokes equation around Re = 0.

Equations (9)–(11) govern the two-dimensional secondary flow across the cross-section. Since the secondary flow is decoupled from the axial flow, we use the stream function (ψ) formulation to determine the secondary velocity field. We define

$$\bar{u} = \frac{\partial\bar{\psi}}{\partial\bar{y}}, \quad (16)$$

$$\bar{v} = -\frac{\partial\bar{\psi}}{\partial\bar{x}}, \quad (17)$$

where, $\bar{\psi}$ is the dimensionless stream function and defined as $\bar{\psi} = \frac{\psi}{U_{ch}x_{ch}}$.

Substituting Eqs. (16) and (17) into Eqs. (10) and (11) and eliminating $\bar{P}$ leads to the following fourth-order partial

TABLE I. Values of parameters used in the simulation [25].

Parameter	Value
Width of microchannel	200 μm
Height of microchannel	200 μm
Applied axial pressure gradient	500 Pa/m
Absolute temperature of solution	298 K
Viscosity of solution	$0.9 * 10^{-3}$ kg/m s
Density of solution	1000 kg/m^3
Zeta potential	−200 mV
Electrolyte concentration of solution	10^{-6} M
Valance of ions in solution	1
Dielectric constant of solution	80

differential equation for the stream function:

$$\frac{\partial^4\bar{\psi}}{\partial\bar{x}^4}+2\frac{\partial^4\bar{\psi}}{\partial\bar{x}^2\partial\bar{y}^2}+\frac{\partial^4\bar{\psi}}{\partial\bar{y}^4}=-G_x\frac{\partial\bar{\rho}_e}{\partial\bar{y}}+G_y\frac{\partial\bar{\rho}_e}{\partial\bar{x}}. \quad (18)$$

The boundary conditions in Eq. (13) translate to the following conditions on $\bar{\psi}$:

$$\begin{aligned}
\bar{\psi}&=\frac{\partial\bar{\psi}}{\partial\bar{x}}=0 \quad \text{at} \quad \bar{x}=0 \quad \text{for} \quad 0<\bar{y}<\lambda,\\
\bar{\psi}&=\frac{\partial\bar{\psi}}{\partial\bar{x}}=0 \quad \text{at} \quad \bar{x}=1 \quad \text{for} \quad 0<\bar{y}<\lambda,\\
\bar{\psi}&=\frac{\partial\bar{\psi}}{\partial\bar{y}}=0 \quad \text{at} \quad \bar{y}=0 \quad \text{for} \quad 0<\bar{x}<1,\\
\bar{\psi}&=\frac{\partial\bar{\psi}}{\partial\bar{y}}=0 \quad \text{at} \quad \bar{y}=\lambda \quad \text{for} \quad 0<\bar{x}<1. \quad (19)
\end{aligned}$$

The nonlinear system of Eqs. (7), (8), (18), and (19) are solved numerically using a finite difference scheme. The spatial derivatives are discretised using a second-order central difference approximation. The fully developed velocity field is obtained by setting G_y to zero in HC1 and G_x to zero in HC2. Inspection of governing equations reveals that the flow depends on the imposed pressure gradient, the applied electric field and solution properties. The number of grids used in each of the x and y directions is 200, beyond which the flow field is unaffected with the increase in number of grids.

The geometric dimensions of the microchannel, operating conditions and properties of the solution used in the simulations are given in Table I. The corresponding dimensionless variables are $\lambda = 1$, $K = 651.3$, and $\bar{\zeta} = -7.785$. These are the values used for all calculations in this work.

IV. VELOCITY FIELD

A. Electric field in the horizontal or x direction

We first consider the case when the electric field is applied only along the horizontal or x direction for the entire length of the mixer. The fluid in the positively charged EDL experiences a body force near the top and bottom walls. The fluid near the walls $\bar{y} = 0$ and 1 is dragged by the applied electric field in the positive x direction. When the fluid reaches the right wall, it turns back and flows (recirculates) along the center line of the channel. This results in a symmetric secondary circulatory flow in the form of two horizontal counter rotating vortices across the cross-section as shown in Fig. 2(a).

These vortices enhance transverse mixing in the microchannel. These counter-rotating vortices formed due to electroosmotic effects are similar to Dean vortices that are induced by centrifugal forces in a curved microchannel. Dean vortices have been studied extensively in the design of micromixers [20,21,26]. Electro-osmotically induced vortices offer two advantages over Dean vortices in micro- mixing applications: (i) The channels here can be straight which allows for a simple design of a microfluidic chip. (ii) The strength of Dean vortices depends on the axial flow velocity and the curvature. In contrast, the strength of electro-osmotically induced vortices can be controlled independent of axial velocity by adjusting the strength of the electric field. This allows for an independent and better control over mixing characteristics.

This secondary flow along with the primary axial flow leads to a helical motion of particles in the flow field as shown in Fig. 2(b). This figure shows the path lines of two particles initially located at (0.1, 0.1) and (0.1, 0.9). Each particle stays in one half of the cross section. The drawback associated with the symmetric structure of the secondary flow is that the particles starting in the top (bottom) half can never cross over into the bottom (top) half of the channel. Hence, in this sense the mixing is poor across the cross-section.

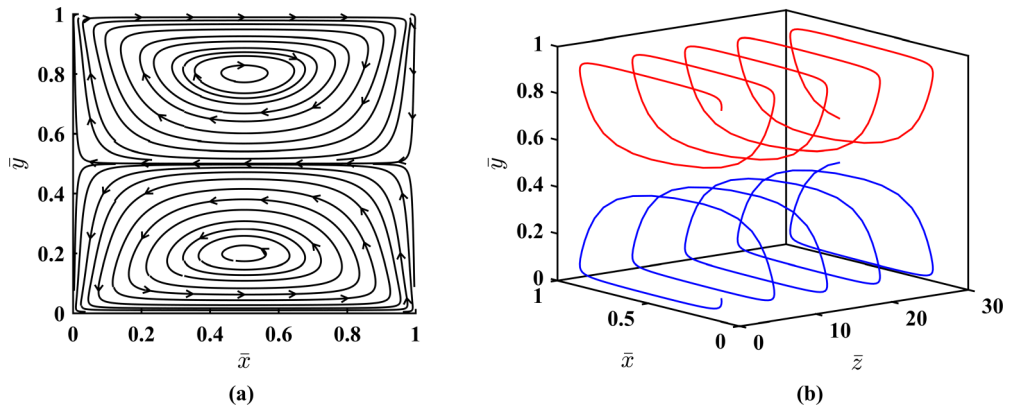

FIG. 2. (a) The streamlines of the secondary flow for a horizontally directed applied electric field, i.e., the streamlines of flow projected onto the cross-section. (b) Path lines of two particles along the length with the initial positions at (0.1, 0.1) and (0.1, 0.9). Each particle remains confined to one half of the channel. $G_x = 1930$.

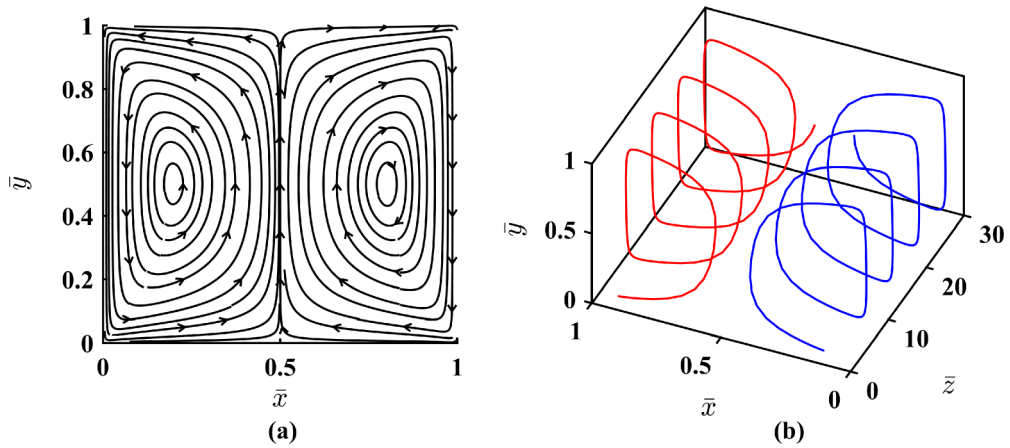

FIG. 3. (a) The streamlines of the secondary flow for a vertically applied electric field, i.e., the streamlines of flow projected onto the cross-section. (b) Path lines of fluid particles along the length with the initial positions at (0.1, 0.1) and (0.9, 0.1). They remain confined to their respective half of the channel. $G_y = -1930$.

B. Electric field in the vertical or *y* direction

In this section, we consider the case when the electric field is applied only along the vertical or y direction for the entire length of the mixer. The fluid in the positively charged EDL experiences a strong body force near the right and left walls. Hence, two vertical counter rotating vortices are formed as depicted in Fig. 3(a). The corresponding helical path lines of the particles is shown in Fig. 3(b). This figure shows the path lines of two particles initially located at (0.1, 0.1) and (0.9, 0.1). Here the particles starting in the left (right) half cannot cross into the right (left) half of the channel, and vice versa. This again limits the mixing efficiency of the microchannel.

C. Periodically applied electric field

To overcome the limitations of mixing when the electric field is unidirectional, we propose periodically changing the direction of the applied electric field, along the length of the channel as shown in Fig. 1. The change in the direction of the applied electric field results in a change in the orientation of the secondary vortices by 90° from one half cell to the next half cell. Now the secondary streamlines of one half cell overlap with those of next half cell. The projection of the streamlines in the two half cells depicting this intersection is shown in Fig. 4. This periodically varying flow pattern leads to chaotic advection of the fluid in which two particles that start out very close to each other, diverge away exponentially quickly as they flow along the channel [27]. This property causes fluid parcels to mix and significantly reduces the effective path length for molecular diffusion. The effect of the periodically rotated electric field on particle paths is shown in Fig. 4(b). The particles are no longer confined to one half of the channel and can move across the entire cross-section. This results in improved mixing when compared to the case of a uniform electric field.

V. MIXING CHARACTERIZATION

In the earlier section, we have shown how the proposed system shows intersection of streamlines and can be a good mixer. We now focus on qualitative and quantitative methods

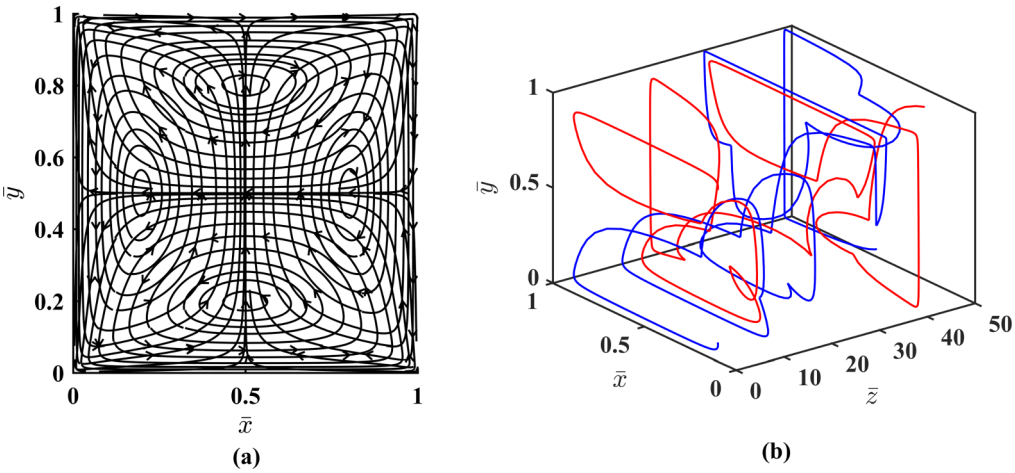

FIG. 4. (a) The crossing of the streamlines for the periodic electric field seen by projecting the streamlines of the individual electric fields. (b) Particle paths in a channel subjected to the periodic electric field with the initial position (0.1, 0.1) and (0.9, 0.1). The particles are no longer confined to the half of the channel in which they started. Instead they are transported throughout the cross section, leading to much better mixing. $G_x = 1930$, $G_y = -1930$, $\bar{z}_l = 5$.

to characterize mixing. For this, two traditional Lagrangian techniques based on Poincaré sections and, Shannon entropy are used. In addition to this, the species transport equation is also used to get physical insight into mixing in the proposed system, and understand the influence of molecular diffusion.

A. Poincaré sections

To investigate the mixing quality in the proposed microchannel, we study the dynamics of passive tracer particles, whose three-dimensional motion is governed by

$$\frac{d\bar{x}}{d\bar{t}} = \bar{u} = \frac{\partial\bar{\psi}}{\partial\bar{y}}, \tag{20}$$

$$\frac{d\bar{y}}{d\bar{t}} = \bar{v} = -\frac{\partial\bar{\psi}}{\partial\bar{x}}, \tag{21}$$

$$\frac{d\bar{z}}{d\bar{t}} = \bar{w}. \tag{22}$$

We are primarily interested in understanding the mixing that occurs across the channel cross-section, which depends on motion in the x-y plane, as given by Eqs. (20) and (21). These two equations form a one degree of freedom Hamiltonian system, with the streamfunction $\bar{\psi}$ as the Hamiltonian. A qualitative picture of the cross-sectional mixing may be obtained from Poincaré maps. As the channel is composed of a series of repeating unit cells, a natural choice for constructing Poincaré maps is to sample the particle trajectories at the end of each unit cell. However, because the axial velocity $\bar{w}$ varies across the cross-section, the time required for each particle to reach the end of a unit cell will depend on their $(\bar{x},\bar{y})$ position at the beginning of the unit cell. The required time can be obtained by using Eq. (22) for the axial position of the particle. It should be noted that the particle dynamics with respect to axial position is *not* formally described by a Hamiltonian system, due to the dependence of $\bar{w}$ on $(\bar{x},\bar{y})$. Nevertheless, many concepts used to understand mixing in two-dimensional unsteady Hamiltonian flows are found to be useful in understanding mixing in three-dimensional steady flows, where particle paths are given by Eqs. (20)–(22) [20].

We now describe the computational procedure followed to construct the Poincare maps. When the horizontally and vertically applied electric fields alternate, the secondary flow field is given by

$$\begin{aligned}\bar{u} &= f_I(\bar{z})\bar{u}_I(\bar{x},\bar{y}) + f_{II}(\bar{z})\bar{u}_{II}(\bar{x},\bar{y}),\\ \bar{v} &= f_I(\bar{z})\bar{v}_I(\bar{x},\bar{y}) + f_{II}(\bar{z})\bar{v}_{II}(\bar{x},\bar{y}),\end{aligned} \tag{23}$$

where subscripts I and II correspond to the flow field when the electric field is applied horizontally and vertically, respectively, in each half cell. In the above,

$$f_I(\bar{z}) = \begin{cases} 1 & m\bar{z}_l < \bar{z} < m\bar{z}_l + \bar{z}_l \\ 0 & m\bar{z}_l + \bar{z}_l < \bar{z} < m\bar{z}_l + 2\bar{z}_l \end{cases}, \tag{24}$$

and

$$f_{II}(\bar{z}) = \begin{cases} 0 & m\bar{z}_l < \bar{z} < m\bar{z}_l + \bar{z}_l \\ 1 & m\bar{z}_l + \bar{z}_l < \bar{z} < m\bar{z}_l + 2\bar{z}_l \end{cases}, \tag{25}$$

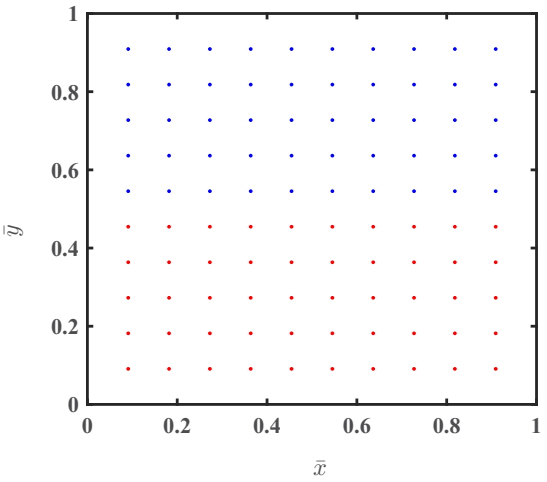

FIG. 5. Initial positions of the 100 passive particles used to determine the Poincaré sections. These passive particles are initially distributed on a uniform grid across the cross-section.

where $m = 0,2,4,\ldots$ represents the set of even integers. Equations (24) and (25) can be viewed as being an on-off and the resulting flow field is spatially periodic with a periodicity $2\bar{z}_l$.

The trajectories of the passive particles are calculated by dividing Eqs. (20) and (21) by Eq. (22). Using Eq. (23), this yields

$$\frac{d\bar{x}}{d\bar{z}} = \frac{f_I(\bar{z})\bar{u}_I(\bar{x},\bar{y}) + f_{II}(\bar{z})\bar{u}_{II}(\bar{x},\bar{y})}{\bar{w}}, \tag{26}$$

$$\frac{d\bar{y}}{d\bar{z}} = \frac{f_I(\bar{z})\bar{v}_I(\bar{x},\bar{y}) + f_{II}(\bar{z})\bar{v}_{II}(\bar{x},\bar{y})}{\bar{w}}. \tag{27}$$

The Poincare sections help determine the position of particles entering the first half of a unit cell when they exit the second half of the unit cell. The mapping is found by numerical integration of Eqs. (26) and (27) using the ode23s solver of Matlab. The velocities required in these equations at a particular location, are determined using the griddedInterpolant function of Matlab. Note that while the 2D map thus constructed is one-to-one and invertible, it is not area preserving because $[\frac{\partial}{\partial\bar{x}}(\bar{u}/\bar{w}) + \frac{\partial}{\partial\bar{y}}(\bar{v}/\bar{w})]$ is nonzero.

At the entrance of the first unit cell, hundred passive particles are uniformly distributed as shown in Fig. 5, This was found to be sufficient to capture the full structure of Poincare section. The particle position are tracked for 500 unit cells to study the long-time dynamics along the axial direction. The Poincare sections were found to be invariant beyond 100 unit cells. However, in order to approximate the infinite-time Poincare map more closely, the results are depicted after 500 unit cells. Figure 6 presents Poincare sections for different lengths of each unit cell. Both chaotic and regular regions are observable in these maps. The extent of these regions depends on the magnitudes of the applied electric fields (in the horizontal and vertical directions), the pressure gradient along the channel, and the length of each unit cell.

A Kolmogorov-Arnold-Moser (KAM) surface is seen to separate the chaotic region from the regular regions, which are periodic orbits [27]. The KAM surface acts as a barrier across which fluid particles cannot be transported. The particles that

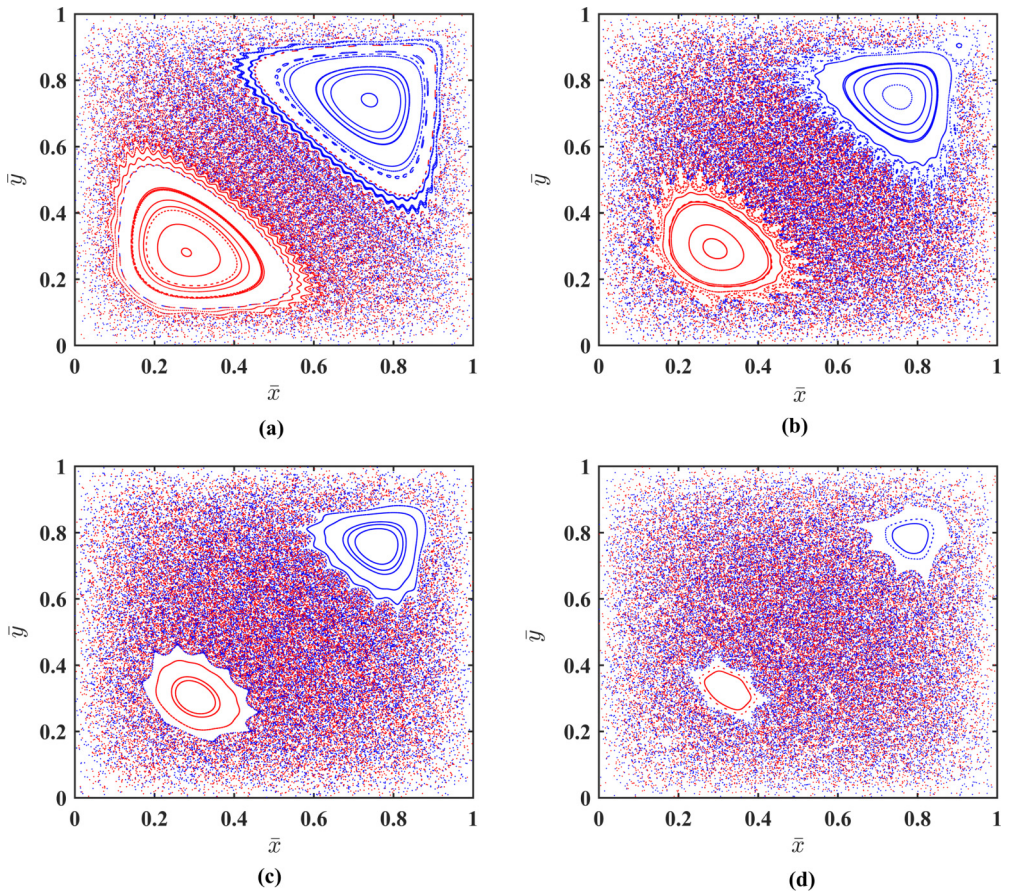

FIG. 6. The Poincaré sections for the periodically applied electric field for varying unit cell length (a) $\bar{z}_l = 2$, (b) $\bar{z}_l = 4$, (c) $\bar{z}_l = 6$, (d) $\bar{z}_l = 10$. $G_x = 193$, $G_y = -193$ for all the cases with the initial condition shown in Fig. 5.

are trapped inside the KAM surface cannot mix with those outside. Thus, the presence of these surfaces implies that mixing does not occur over the entire domain. The particle trajectories in the chaotic region exhibit chaotic dynamics. Here, a particle on visiting a particular neighbourhood follows a trajectory that diverges exponentially from the trajectory followed after their earlier visit to the same neighborhood.

We see that there exist a number of periodic orbits at small unit cell length ($\bar{z}_l$), which disintegrate on increasing the unit cell length. This leads to an increase in the chaotic region as depicted in Fig. 6. As the unit cell length is increased from $\bar{z}_l = 2$ to $\bar{z}_l = 4$, the outer KAM surfaces are destroyed and the area of chaotic sea increases. As we further increase $\bar{z}_l$ almost all periodic orbits are destroyed and the chaotic region is further increased.

As mentioned above, the nature of Poincare sections depends on the magnitude and the direction of the applied electric field. Poincare sections obtained by increasing the magnitude of G_x and G_y are shown in Figs. 7 and 8, for different $\bar{z}_l$. When the horizontally applied electric field (G_x) alone is increased (for a given $\bar{z}_l$ and G_y), the chaotic region increases as can be observed by comparing Figs. 6 and 7. When we increase the electric field in both the directions, chaotic regions are further enhanced as shown in Fig. 8. Considering Figs. 6, 7, and 8, it can be concluded that on increasing $\bar{z}_l$, the chaotic region increases for any given G_x and G_y. However, the influence of $\bar{z}_l$ on the chaotic region is less significant when the applied electric field is high. Further, we can observe in Fig. 7 that the regular region shifts with increase in $\bar{z}_l$.

The Poincare maps analyzed in this section give qualitative insight about the chaotic mixing. However, it does not give any quantitative estimate of the extent of mixing. This is the subject of the next section.

B. Shannon entropy

Poincare maps yield only qualitative information on mixing. In contrast Shannon entropy is a measure which helps quantify the extent of mixing. This is also based on the Lagrangian approach. This quantification is independent of the physical process responsible for mixing and relies only on the information of entropy. This can be used to analyse data from numerical simulations, as well as experiments.

Shannon entropy was calculated following Camesasca *et al.* [28] using particle positions at the end of every unit cell. Particle positions are calculated using Eqs. (26) and (27). The microchannel cross section is divided into several regions called bins. Each bin is denoted by $j = 1,2,\ldots,M$. Let there be "c" species where $c = 1,2,\ldots,C$. We calculate the probability distribution of each species in each bin. This is used to calculate the Shannon entropy, which is given by

$$S = -\sum_{j=1}^{M}\sum_{c=1}^{C} p_{j,c} \ln p_{j,c}. \tag{28}$$

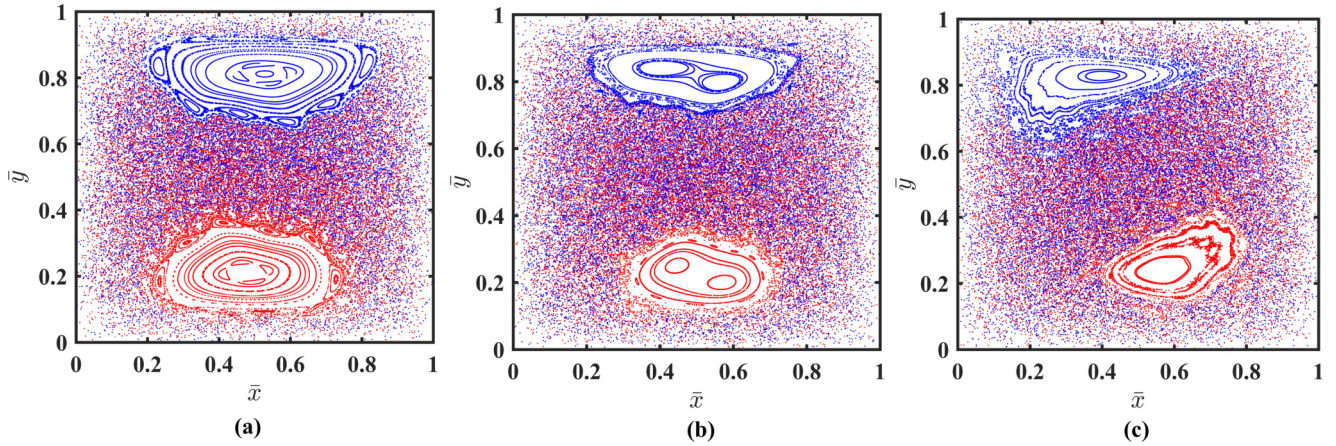

FIG. 7. The Poincaré sections for the periodically applied electric field for varying unit cell length (a) $\bar{z}_l = 2$, (b) $\bar{z}_l = 4$, (c) $\bar{z}_l = 6$. $G_x = 1930$, $G_y = -193$ are the constants for all the cases with the initial condition shown in Fig. 5.

Here $p_{j,c}$ is the joint probability that a particle of species c is located in bin j. It is given by

$$p_{j,c} = \frac{\frac{n_{j,c}}{P_c}}{\sum_{i=1}^{M}\sum_{c=1}^{C}\frac{n_{i,c}}{P_c}}, \tag{29}$$

where $n_{j,c}$ is the number of particles of species c in bin j and P_c is the total number of particles of species c in all the bins.

The total entropy is additive and can be written as a sum of the entropy of spatial distribution S(location) and the conditional entropy S_{location}(species). S(location) is the entropy associated with the spatial distribution of particles irrespective of species and is given by

$$S(\text{location}) = -\sum_{j=1}^{M} p_j \ln p_j, \tag{30}$$

where p_j is the probability that a group of particles, irrespective of species is in bin j and it is given by

$$p_j = \frac{\sum_{c=1}^{C}\frac{n_{j,c}}{P_c}}{\sum_{i=1}^{M}\sum_{c=1}^{C}\frac{n_{i,c}}{P_c}}. \tag{31}$$

S_{location}(species) is given by

$$S_{\text{location}}(\text{species}) = -\sum_{j=1}^{M} p_j \sum_{c=1}^{C} p_{c/j} \ln p_{c/j}. \tag{32}$$

S_{location}(species) is an average over the M spatial bins and signifies the entropy of mixing, that the species c is conditional on being in bin j. Here $p_{c/j}$ is the conditional probability that a group of particles of species c is in bin j is given by

$$p_{c/j} = \frac{\frac{n_{j,c}}{P_c}}{\sum_{c=1}^{C}\frac{n_{j,c}}{P_c}}. \tag{33}$$

S(location) quantifies the spatial homogeneity of the particles irrespective of the species, whereas S_{location}(species) quantifies the quality of mixing of the species conditional on locations. S(location) and S_{location}(species) are normalized by $\ln M$ and $\ln C$, respectively (the maximum of S(location) and S_{location}(species), respectively).

For our computations, we have considered 1600 particles of two species (red and blue). The red and blue particles are placed at the bottom and top halves, respectively, at $\bar{z} = 0$. Hence, initially there is uniform distribution of particles. Consequently, S(location) is maximum and is unity. There

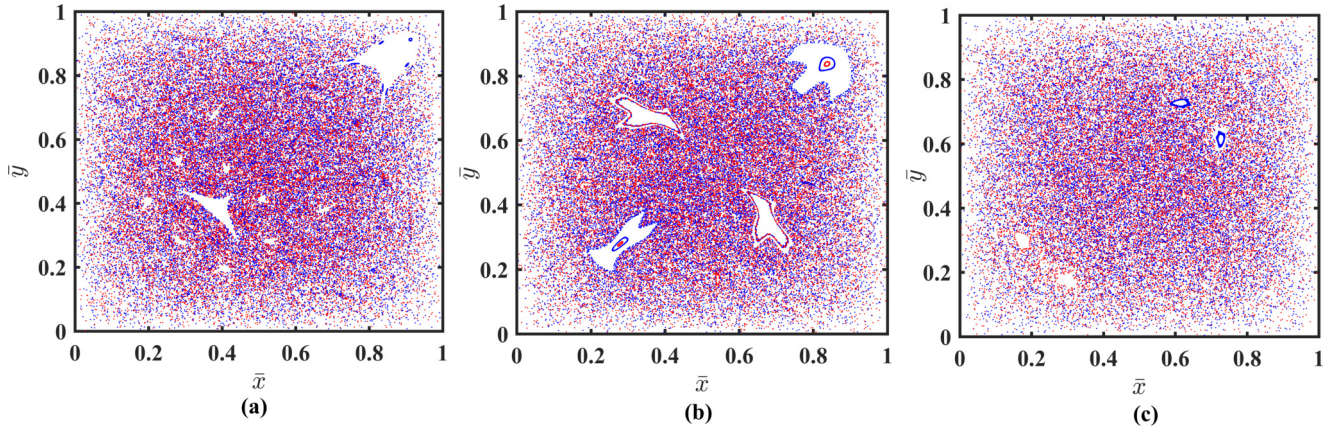

FIG. 8. The Poincaré sections for the periodically applied electric field for varying unit cell length (a) $\bar{z}_l = 2$, (b) $\bar{z}_l = 4$, (c) $\bar{z}_l = 6$. $G_x = 1930$, $G_y = -1930$ are the constants for all the cases with the initial condition shown in Fig. 5.

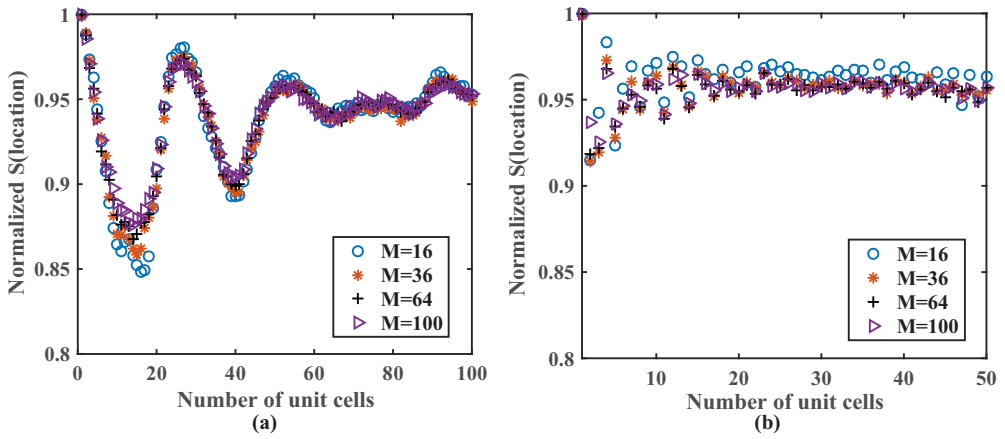

FIG. 9. Variation of normalized S(location) with number of unit cells for (a) $G_x = 193$, $G_y = -193$. (b) $G_x = 1930$, $G_y = -1930$, and $\bar{z}_l = 2$ for different number of bins (M). The normalized S(location) is independent of number of bins. The corresponding Poincare maps are depicted in Figs. 6(a) and 8(a), respectively.

also exists a perfect segregation of species for a given bin, so S_{location}(species) is zero. Mixing is quantified using Shannon entropy for conditions for which Poincare sections are depicted in Figs. 6(a) and 8(a), respectively. These correspond to qualitatively low and high mixing, represented by case I and case II, respectively, in the following.

Figure 9 shows the variation of normalized S(location) with number of unit cells, for different number of bins. Figure 9(a) corresponds to case I, wherein mixing is relatively poor, while Fig. 9(b) corresponds to case II, wherein mixing is superior (cf. the Poincaré maps in Figs. 6(a) and 8(a), respectively). The value of S(location) undergoes a series of decaying oscillations until it reaches an asymptotic value of around 0.95, which indicates that the spatial distribution of particles after a sufficient number of unit cells is very nearly uniform, although not exactly so. In both cases, the normalized S(location) is almost independent of the number of bins used in the calculation.

While the asymptotic values of S(location) are nearly the same for both cases I and II, the number of unit cells required to attain this value is much less in case II, which corresponds to better mixing. In case I, Fig. 9(a) shows that S(location) undergoes large oscillations which gradually decay with the number of unit cells. The underlying reason for these oscillations is that the 2D dynamical system given by Eqs. (26) and (27) is not area preserving. This follows from the dependence of the axial velocity $\bar{w}$ on the $\bar{x}, \bar{y}$ position in the cross-section, due to which the divergence of the vector field $[\frac{\partial}{\partial \bar{x}}(\bar{u}/\bar{w}) + \frac{\partial}{\partial \bar{y}}(\bar{v}/\bar{w})]$ is nonzero, although $[\frac{\partial \bar{u}}{\partial \bar{x}} + \frac{\partial \bar{v}}{\partial \bar{y}}] = 0$. As a result of this non-area-preserving property, particles get concentrated in certain regions of the cross-section (negative divergence of the vector field), while they get dispersed in others (positive divergence). Figure 10 shows the divergence of the vector field for the two half-cells, along with the corresponding streamlines. As particles flow along the channel, some of them may experience a predominantly convergent (divergent) vector field $[(\bar{u}/\bar{w}),(\bar{v}/\bar{w})]$, due to which they get concentrated (dispersed) and result in a decrease (increase) of S(location).

The spatial distribution of particles at various locations along the channel (number of unit cells) is shown in Fig. 11. These are the particle distributions that are used to calculate S(location). It can be seen that within the first few unit cells, particles get concentrated into a clump near the bottom-right of the cross-section. This clump persists for about the first 15 unit cells, and results in the initial sharp decrease of S(location) seen in Fig. 9(a). Subsequently, the concentrated patch of

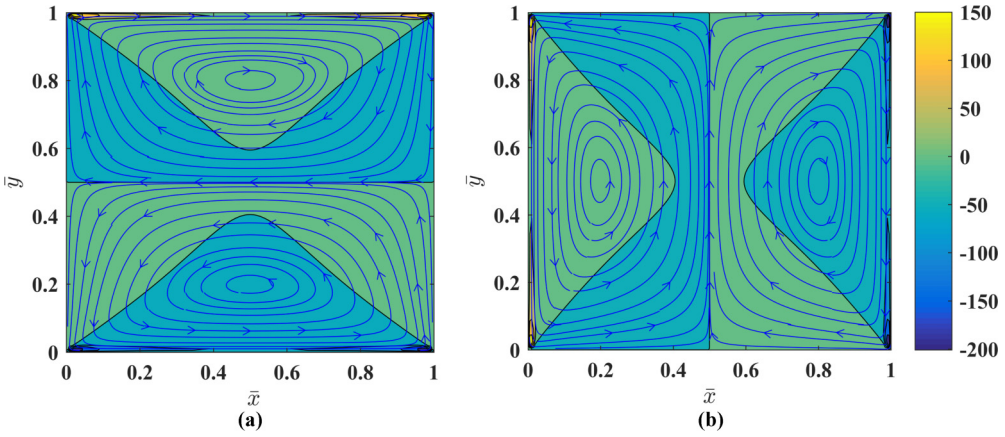

FIG. 10. The divergence of vector field $[(\bar{u}/\bar{w}),(\bar{v}/\bar{w})]$ for the (a) first half cell and (b) second half cell along with the stream line plot.

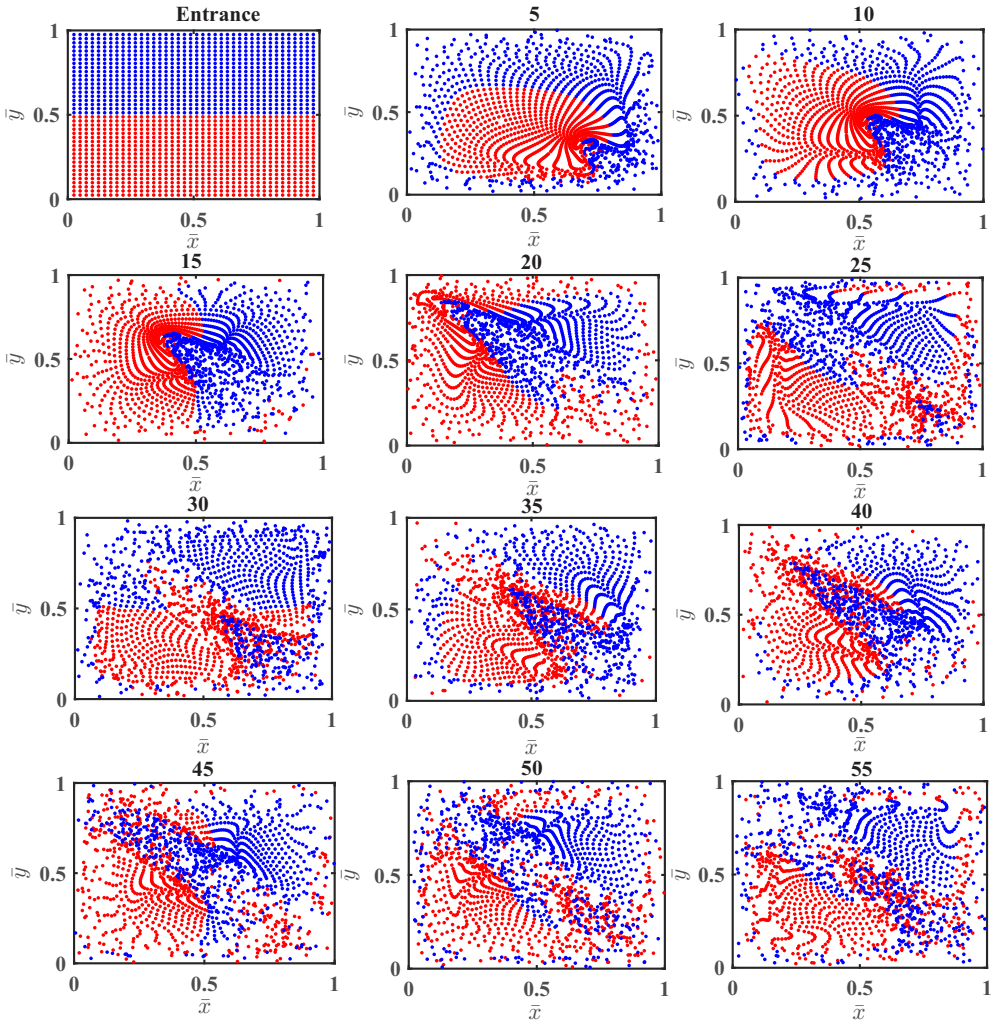

FIG. 11. The spatial distribution of particles along the length of the channel (number of unit cell) for the case I. The number of unit cells corresponding to each spatial distribution is mentioned above the respective panel.

particles is advected across the channel into the top-left corner, where it gets dispersed under the action of a predominantly divergent vector field. This leads to the rise of S(location) between unit cells 18 to 30 in Fig. 9(a). This process repeats itself, but with a reduced agglomeration of particles each time. This results in decaying oscillations of S(location), which ultimately attains a relatively unchanging asymptotic value. The degree of these oscillations is much less in Fig. 9(b), because the chaotic region of the Poincare map is much larger in this case [compare Figs. 6(a) and 8(a)]. Therefore, particles are able to sample larger regions of the flow field more rapidly. Consequently, the divergence of the vector field experienced by them fluctuates too quickly for any significant amount of agglomeration to take place.

To verify that the oscillations of S(location) are due to the dependence of the axial velocity on the $\bar{x},\bar{y}$ position, we have recalculated S(location) after replacing the axial velocity with its cross-sectional average value (which is independent of position). The corresponding vector field is divergence free and area preserving. The result for case I, corresponding to Fig. 9(a), is depicted in Fig. 12, which shows that S(location) remains close to unity without any significant oscillations, for all bin numbers.

Next, we analyze the variation of normalized S_{location}(species) with the number of unit cells. The results for case I, considering different number of bins, is shown in Fig. 13(a). For this case, as the extent of mixing is less, S_{location}(species) has not reached the maximum value of unity when the number of bins is 100, but rather has a much lower value of 0.62. In this case, the region occupied by islands in the Poincaré map is more than the region of the chaotic sea [cf. Fig. 6(a)], as a result of which interspecies mixing is low. Consequently, it requires a greater number of unit cells, or an increase in unit cell length, to achieve good mixing. Figure 13(b) depicts the variation of normalized S_{location}(species) for case II, in which the chaotic region of the Poincaré map is much larger [cf. Fig. 8(a)]. Here, S_{location}(species) approaches a value close to unity, within 20 unit cells, which indicates more rapid and uniform interspecies mixing. In both these cases, the normalized S_{location}(species) is dependent on the number of bins and the maximum value is observed for fewer bins. The entropy of mixing decreases

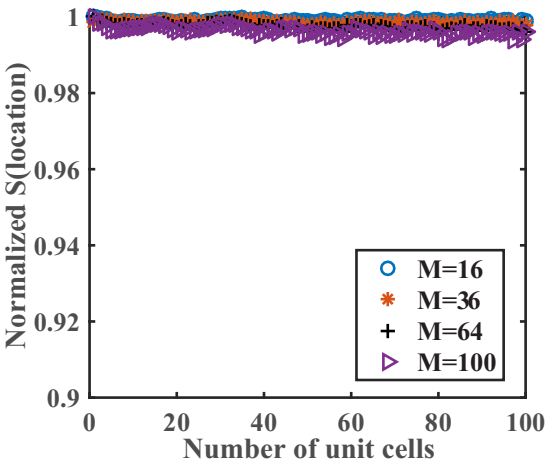

FIG. 12. Variation of normalized S(location) with number of unit cells for $G_x = 193$, $G_y = -193$, and $\bar{z}_l = 2$ for different number of bins (M) with the axial velocity replaced by its cross-sectional average value. The normalized S(location) is independent of number of bins and particle distribution is uniform.

with increase in the number of bins, i.e., when the system is analyzed at smaller scales. This indicates that the composition of the two species varies with the scale of observation.

When the number of bins is low, i.e., 16, we see an oscillatory response of S_{location}(species), especially for low electric fields. Unlike the oscillations of S(location), these oscillations are *not* related to the non-area-preserving nature of Eqs. (26) and (27). They are found to persist even when the cross-sectional average of the axial velocity is used in the calculation, instead of the spatially varying axial velocity. On the other hand, the amplitude of the oscillations decreases as the number of bins increases, until a relatively monotonic variation is obtained. This implies that the oscillations of S_{location}(species) are an artifact of low resolution, i.e., having too few bins.

From the behavior of S(location) and S_{location}(species), we conclude that mixing is more uniform for high applied electric fields. The number of unit cells required for a particular extent of mixing is low when the applied electric field is high.

C. Species transport equation

In the previous sections, we discussed the use of Poincare maps and Shannon entropy to estimate the extent of mixing. In this section, we analyze another measure, which is based on using the scalar transport of a species to quantify mixing. At steady state, the scalar species transport equation is given by

$$u\frac{\partial C}{\partial x} + v\frac{\partial C}{\partial y} + w\frac{\partial C}{\partial z} = D\left(\frac{\partial^2 C}{\partial x^2} + \frac{\partial^2 C}{\partial y^2} + \frac{\partial^2 C}{\partial z^2}\right), \quad (34)$$

where C is the concentration of the species and D is the diffusivity of the species. We neglect diffusion along the flow direction, as the advection in flow direction dominates the diffusion process. Under these conditions, the dimensionless species transport equation is given by

$$\bar{u}\frac{\partial \bar{C}}{\partial \bar{x}} + \bar{v}\frac{\partial \bar{C}}{\partial \bar{y}} + \bar{w}\frac{\partial \bar{C}}{\partial \bar{z}} = \frac{1}{\text{Pe}}\left(\frac{\partial^2 \bar{C}}{\partial \bar{x}^2} + \frac{\partial^2 \bar{C}}{\partial \bar{y}^2}\right). \quad (35)$$

This equation is subject to the following boundary conditions

$$\begin{aligned}
&\frac{\partial \bar{C}}{\partial \bar{x}} = 0 \quad \text{at} \quad \bar{x} = 0 \quad \text{for} \quad 0 < \bar{y} < \lambda,\\
&\frac{\partial \bar{C}}{\partial \bar{x}} = 0 \quad \text{at} \quad \bar{x} = 1 \quad \text{for} \quad 0 < \bar{y} < \lambda,\\
&\frac{\partial \bar{C}}{\partial \bar{y}} = 0 \quad \text{at} \quad \bar{y} = 0 \quad \text{for} \quad 0 < \bar{x} < 1,\\
&\frac{\partial \bar{C}}{\partial \bar{y}} = 0 \quad \text{at} \quad \bar{y} = \lambda \quad \text{for} \quad 0 < \bar{x} < 1,\\
&\text{and} \quad \bar{C} = \bar{C}_0 \quad \text{at} \quad \bar{z} = 0. \qquad (36)
\end{aligned}$$

In the above equations, $\bar{C} = \frac{C}{C_0}$ and $\text{Pe} = \frac{U_{ch}x_{ch}}{D}$. Equations (35) and (36) are solved numerically using an operator splitting method [29]. Here $\bar{z}$ is treated as analogous to time since fluid always moves forward in $\bar{z}$. In the operator splitting method the species transport by convection and diffusion is

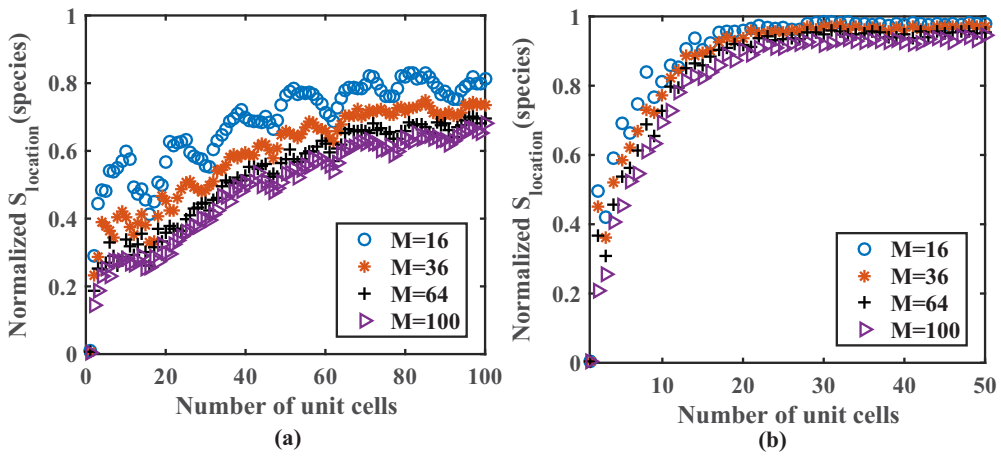

FIG. 13. Variation of normalized S_{location}(species) with number of unit cells for (a) $G_x = 193$, $G_y = -193$. (b) $G_x = 1930$, $G_y = -1930$, and $\bar{z}_l = 2$ for different number of bins (M). The behavior of normalized S_{location}(species) is dependent on the number of bins and a higher value is obtained for fewer number of bins.

considered sequentially in each direction, over a given time interval. After calculating convection and diffusion steps in a particular time interval, the time step is advanced and the process is repeated.

To implement this method, Eq. (35) is divided into four differential equations, where only one transport step is considered at a time as shown below.

$$\text{Diffusion in } x \text{ direction} : \bar{w}\frac{\partial \bar{C}_1}{\partial \bar{z}} = \frac{1}{\text{Pe}}\frac{\partial^2 \bar{C}_1}{\partial \bar{x}^2}, \tag{37}$$

$$\text{Diffusion in } y \text{ direction} : \bar{w}\frac{\partial \bar{C}_2}{\partial \bar{z}} = \frac{1}{\text{Pe}}\frac{\partial^2 \bar{C}_2}{\partial \bar{y}^2}, \tag{38}$$

$$\text{Advection in } x \text{ direction} : \bar{w}\frac{\partial \bar{C}_3}{\partial \bar{z}} + \bar{u}\frac{\partial \bar{C}_3}{\partial \bar{x}} = 0, \tag{39}$$

$$\text{Advection in } y \text{ direction} : \bar{w}\frac{\partial \bar{C}_4}{\partial \bar{z}} + \bar{v}\frac{\partial \bar{C}_4}{\partial \bar{y}} = 0. \tag{40}$$

In an interval $d\bar{z}$, Eq. (37) is solved first to obtain $\bar{C}_1$ with the initial condition given by Eq. (36) for $\bar{C}_0$. We then solve for $\bar{C}_2$ using Eq. (38) with the initial condition as $\bar{C}_1$. Similarly $\bar{C}_3$ is obtained by solving Eq. (39) with the initial condition as $\bar{C}_2$ and finally Eq. (40) is solved for $\bar{C}_4$ with the initial condition as $\bar{C}_3$. This is solved sequentially in an interval $d\bar{z}$ to find the concentration $\bar{C}$. The time ($\bar{z}$) is then advanced to the next step.

The transport by diffusion in the x and y directions is solved numerically using an explicit second order central difference approximation. The numerical algorithm for the purely advection equations in x and y directions have to ensure that no errors arise by artificial diffusion. Different numerical schemes for solving these hyperbolic equations are discussed in the literature [30]. Traditional first order upwind and Lax-Friedrichs schemes leads to numerical dissipation and the solution obtained is highly diffusive. On the other hand second order schemes such as Lax-Wendroff and QUICK lead to oscillatory solutions due to dispersion. Hence, high resolution schemes such as flux corrected transport (FCT) and total variation diminishing (TVD) schemes have been proposed to minimize the dissipation and dispersion errors. In this work, the TVD scheme [31] based on the finite difference method is employed.

Simulations were performed to study the mixing of a species that has an inlet concentration of $\bar{C}_0 = 1$ and $\bar{C}_0 = 0$ in the upper and lower halves of the domain respectively. A uniform concentration ($\bar{C} = 0.5$) everywhere in the cross-section would signify complete mixing. In order to quantify mixing efficiency, we have used the mixing index, which is

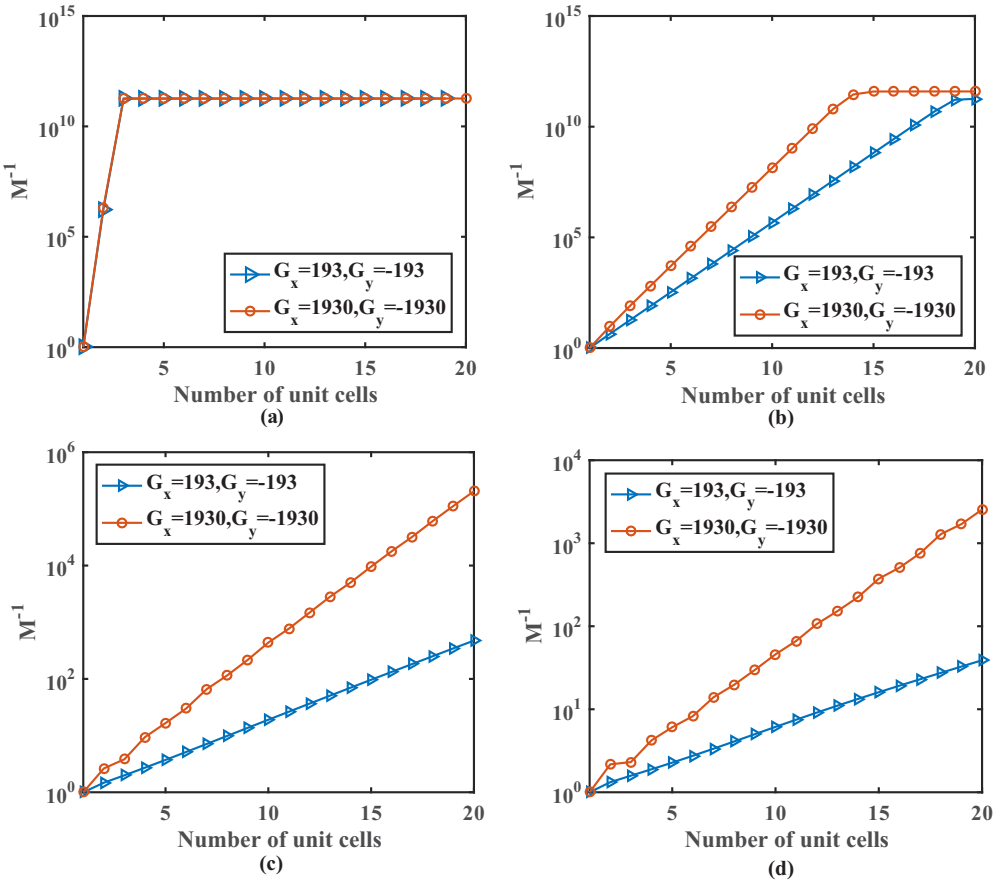

FIG. 14. Variation of inverse mixing index for a periodically altering applied electric field as a function of the number of unit cells for different Péclect numbers for two combinations of G_x and G_y. Here half-cell length is 2. (a) Pe = 100, (b) Pe = 1000, (c) Pe = 5000, (d) Pe = 10000.

based on the deviation of the concentration distribution from a uniform value. This is given as [32]

$$M = \frac{\sigma}{\bar{C}_{\text{avg}}} = \frac{1}{\bar{C}_{\text{avg}}}\sqrt{\langle \bar{C}^2 \rangle - \langle \bar{C} \rangle^2} \simeq \sqrt{\frac{1}{N-1}\sum_{i}^{N}\left(\frac{\bar{C}_i}{\bar{C}_{\text{avg}}} - 1\right)^2}, \quad (41)$$

where, M is the mixing index of the species, σ is the standard deviation, N is the number of nodes (grid points), $\bar{C}_i$ is the concentration at the node i, and $\bar{C}_{\text{avg}}$ is the average concentration of species. Mixing efficiency is defined as

$$\text{Mixing efficiency} = \left(1 - \frac{\sigma}{\bar{C}_{\text{avg}}}\right) \times 100\%. \quad (42)$$

According to the mixing index definition in Eq. (41), perfect mixing results in $M = 0$, since the concentration everywhere is equal the average concentration. Hence, lower values of M indicate better mixing.

For the proposed electroosmotic mixer, the mixing index depends on the length of the unit cell, the applied electric field, and the pressure gradient. Results are depicted in terms of the inverse mixing index (M^{-1}) to facilitate comparison between various cases. Larger values of M^{-1} indicate better mixing.

Figure 14 shows the variation of the inverse mixing index (M^{-1}) with the number of unit cells, for different values of the Peclet number (Pe). In advective mixing, the mixing index decays with the length of the microchannel. Hence, M^{-1} increases exponentially for all Pe and it saturates to a constant value after a certain number of unit cells. Beyond this, there is no further improvement in mixing. Figure 14(a) depicts the variation of M^{-1} for a small Peclet number of Pe = 100, and for two different combinations of G_x and G_y values. It can be seen that an increase in G_x and G_y has no effect on mixing. This is to be expected since for low Pe, diffusion plays a dominant role in species transport as compared to advection.

As we increase Pe, the effect of diffusion on species transport is supressed and advection starts to dominate. Under these conditions mixing is affected by G_x and G_y as shown in Figs. 14(b)–14(d). Figure 14(b) depicts the variation of M^{-1} for Pe 1 000, where both diffusion and advection play a comparable role in species transport. The effect of G_x and G_y is clearly observed in this figure. An increase in G_x and G_y results in a significant increase of M^{-1}, which implies a better mixing of fluids across the cross-section. We further increase Pe to reduce the effect of diffusion as compared to advection on species transport. Figures 14(c) and 11(d) show the variation of M^{-1} for Pe 5 000 and 10 000, respectively. Here M^{-1} decreases with an increase in Pe as mass transfer due to diffusion is negligible. It can be seen that the influence of G_x and G_y become more prominent as Pe is increased.

The length required to achieve a desired degree of mixing depends upon Pe. We define the mixing length as the length required for 95% mixing (i.e., $M = 0.05$). The dependence of the mixing length on Pe is shown in Fig. 15. As expected, the mixing length required increases with an increase in Pe, because the effect of diffusion on species transport is reduced. The dependence of mixing length on Pe generally follows a logarithmic or power law [33] relationship. For the conditions

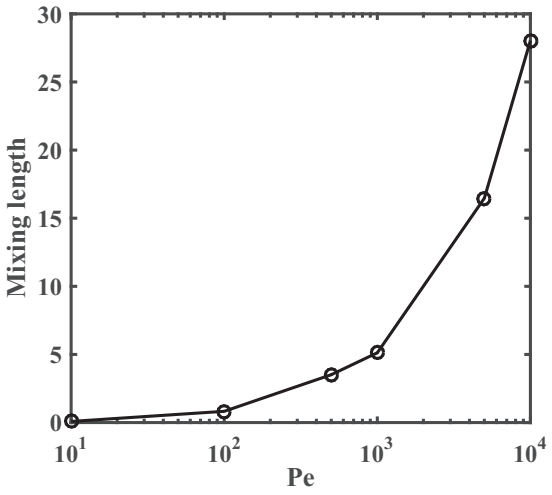

FIG. 15. Variation of mixing length for a periodically altering applied electric field as a function of Péclet number for $G_x = 1930$, $G_y = -1930$, and $\bar{z}_l = 2$ for 95% mixing.

shown in Fig. 14, the mixing length follows the following power law behavior:

$$z_m \alpha \text{Pe}^{0.83}. \quad (43)$$

VI. SUMMARY AND CONCLUSIONS

In this work, we have shown how electro-osmosis induces chaotic mixing in a microchannel. The geometry consists of a straight channel that is subject to an applied electric field with a periodically alternating direction. The primary flow is pressure driven and the transverse flow is electroosmotic. The periodic variation of the electric field along the channel leads to a crossing of streamlines, which in turn is responsible for the chaotic mixing. The concept proposed can be implemented without making any changes to the geometry of an existing microchannel. In fact, the micro channel can have a simple straight geometry.

A common issue encountered in flows driven by electric fields is the occurrence of electrochemical reactions at the electrodes, in case they are in contact with the fluid. These reactions could produce gas bubbles that will interfere with the flow field. One way of overcoming this issue is to use *noncontact electrodes* in the construction of the proposed electro-osmotic mixer. These electrodes will drive a transverse electro-osmotic flow without coming in contact with the fluid [34].

The mixing efficiency of the mixer has been analyzed numerically using Lagrangian techniques, as well as by solving the species transport equation. In the former, the paths of passive tracer particles are tracked and used to obtain Poincaré maps and to calculate Shannon entropy, which provided qualitative and quantitative measures of mixing, respectively. The influence of molecular diffusion on mixing has been studied by solving the species transport equation and analyzing the influence of the Péclet number on the extent of mixing. These different techniques of quantifying mixing lead to a consistent picture of enhanced mixing in the proposed electro-osmotic mixer. Mixing efficiency increases when the

applied electric field strength is increased. Longer unit cells also lead to better mixing.

To conclude, we have proposed a micromixer based on an alternating applied electric field. The performance of this mixer has been theoretically analyzed for different operating conditions by studying the effect of different parameters on the mixing performance.

APPENDIX

The equations governing the system are the continuity equation, the Navier-Stokes equations, and the Poisson-Boltzmann equation. These are nondimensionalized using the characteristic scales [Eqs. (14)] and result in the dimensionless variables given in Eq. (15). The dimensionless continuity and momentum balance equations are

$$\frac{\partial \bar{u}}{\partial \bar{x}} + \frac{\partial \bar{v}}{\partial \bar{y}} + \frac{\partial \bar{w}}{\partial \bar{z}} = 0, \tag{A1}$$

$$\mathrm{Re}\left(\bar{u}\frac{\partial \bar{u}}{\partial \bar{x}} + \bar{v}\frac{\partial \bar{u}}{\partial \bar{y}} + \bar{w}\frac{\partial \bar{u}}{\partial \bar{z}}\right) = -\frac{\partial \bar{P}}{\partial \bar{x}} + \frac{\partial^2 \bar{u}}{\partial \bar{x}^2} + \frac{\partial^2 \bar{u}}{\partial \bar{y}^2} + \frac{\partial^2 \bar{u}}{\partial \bar{z}^2} + G_x \bar{\rho}_e, \tag{A2}$$

$$\mathrm{Re}\left(\bar{u}\frac{\partial \bar{v}}{\partial \bar{x}} + \bar{v}\frac{\partial \bar{v}}{\partial \bar{y}} + \bar{w}\frac{\partial \bar{v}}{\partial \bar{z}}\right) = -\frac{\partial \bar{P}}{\partial \bar{y}} + \frac{\partial^2 \bar{v}}{\partial \bar{x}^2} + \frac{\partial^2 \bar{v}}{\partial \bar{y}^2} + \frac{\partial^2 \bar{v}}{\partial \bar{z}^2} + G_y \bar{\rho}_e, \tag{A3}$$

$$\mathrm{Re}\left(\bar{u}\frac{\partial \bar{w}}{\partial \bar{x}} + \bar{v}\frac{\partial \bar{w}}{\partial \bar{y}} + \bar{w}\frac{\partial \bar{w}}{\partial \bar{z}}\right) = -\frac{\partial \bar{P}}{\partial \bar{z}} + \frac{\partial^2 \bar{w}}{\partial \bar{x}^2} + \frac{\partial^2 \bar{w}}{\partial \bar{y}^2} + \frac{\partial^2 \bar{w}}{\partial \bar{z}^2}, \tag{A4}$$

where, Re is the Reynolds number defined as $\frac{\rho U_{ch} x_{ch}}{\mu}$. The general solution of the nonlinear governing Eqs. (A1)–(A4) is dependent on the Reynolds number Re. In the creeping flow limit, i.e., for low Reynolds numbers (Re < 1), the perturbation approach can be used to obtain an approximate solution to the nonlinear governing equations.

In this approach, the dependence of the solution on Re is explicitly represented as a power series:

$$\bar{u}(\bar{x},\bar{y},\bar{z};\mathrm{Re}) \simeq \bar{u}_0(\bar{x},\bar{y},\bar{z}) + \bar{u}_1(\bar{x},\bar{y},\bar{z})\mathrm{Re} + \bar{u}_2(\bar{x},\bar{y},\bar{z})\mathrm{Re}^2 + O(\mathrm{Re}^3), \tag{A5}$$

$$\bar{v}(\bar{x},\bar{y},\bar{z};\mathrm{Re}) \simeq \bar{v}_0(\bar{x},\bar{y},\bar{z}) + \bar{v}_1(\bar{x},\bar{y},\bar{z})\mathrm{Re} + \bar{v}_2(\bar{x},\bar{y},\bar{z})\mathrm{Re}^2 + O(\mathrm{Re}^3), \tag{A6}$$

$$\bar{w}(\bar{x},\bar{y},\bar{z};\mathrm{Re}) \simeq \bar{w}_0(\bar{x},\bar{y},\bar{z}) + \bar{w}_1(\bar{x},\bar{y},\bar{z})\mathrm{Re} + \bar{w}_2(\bar{x},\bar{y},\bar{z})\mathrm{Re}^2 + O(\mathrm{Re}^3), \tag{A7}$$

$$\bar{P}(\bar{x},\bar{y},\bar{z};\mathrm{Re}) \simeq \bar{P}_0(\bar{x},\bar{y},\bar{z}) + \bar{P}_1(\bar{x},\bar{y},\bar{z})\mathrm{Re} + \bar{P}_2(\bar{x},\bar{y},\bar{z})\mathrm{Re}^2 + O(\mathrm{Re}^3). \tag{A8}$$

We substitute Eqs. (A5)–(A8) into (A1)–(A4) and equate the different powers of Re. This yields a series of linear problems, which have to be solved sequentially to determine the asymptotic solution.

When Re $= 0$, there are no inertial forces acting. Hence, the zeroth-order solution $O(\mathrm{Re}^0)$ corresponds to the creeping flow limit. We refer to this as the base flow. Equating the coefficients of Re^0, we obtain the following equations:

$$\frac{\partial \bar{u}_0}{\partial \bar{x}} + \frac{\partial \bar{v}_0}{\partial \bar{y}} + \frac{\partial \bar{w}_0}{\partial \bar{z}} = 0, \tag{A9}$$

$$\frac{\partial^2 \bar{u}_0}{\partial \bar{x}^2} + \frac{\partial^2 \bar{u}_0}{\partial \bar{y}^2} + \frac{\partial^2 \bar{u}_0}{\partial \bar{z}^2} - \frac{\partial \bar{P}_0}{\partial \bar{x}} + G_x \bar{\rho}_e = 0, \tag{A10}$$

$$\frac{\partial^2 \bar{v}_0}{\partial \bar{x}^2} + \frac{\partial^2 \bar{v}_0}{\partial \bar{y}^2} + \frac{\partial^2 \bar{v}_0}{\partial \bar{z}^2} - \frac{\partial \bar{P}_0}{\partial \bar{y}} + G_y \bar{\rho}_e = 0, \tag{A11}$$

$$\frac{\partial^2 \bar{w}_0}{\partial \bar{x}^2} + \frac{\partial^2 \bar{w}_0}{\partial \bar{y}^2} + \frac{\partial^2 \bar{w}_0}{\partial \bar{z}^2} - \frac{\partial \bar{P}_0}{\partial \bar{z}} = 0. \tag{A12}$$

These equations admit a fully developed flow field when the pressure gradient $\frac{\partial \bar{P}_0}{\partial \bar{z}}$ is a constant. The governing equations used in this work are the zeroth-order solution of the momentum equations.

[1] M. W. Losey, R. J. Jackman, S. L. Firebaugh, M. A. Schmidt, and K. F. Jensen, J. Microelectromech. Syst. **11**, 709 (2002).

[2] K. F. Jensen, AIChE J. **45**, 2051 (1999).

[3] H. A. Stone, A. D. Stroock, and A. Ajdari, Annu. Rev. Fluid Mech. **36**, 381 (2004).

[4] A. Manz, C. S. Effenhauser, N. Burggraf, D. J. Harrison, K. Seiler, and K. Fluri, J. Micromech. Microeng **4**, 257 (1994).

[5] A. D. Stroock, S. K. W. Dertinger, A. Ajdari, I. Mezic, H. A. Stone, and G. M. Whitesides, Science **295**, 647 (2002).

[6] R. H. Liu, M. A. Stremler, K. V. Sharp, M. G. Olsen, J. G. Santiago, R. J. Adrian, H. Aref, and D. J. Beebe, J. Microelectromech. Syst. **9**, 190 (2000).

[7] S. Qian and H. H. Bau, Anal. Chem. **74**, 3616 (2002).

[8] N.-T. Nguyen and Z. Wu, J. Micromech. Microeng **15**, R1 (2005).

[9] C. Y. Lee, C. L. Chang, Y. N. Wang, and L. M. Fu, Int. J. Mol. Sci. **12**, 3263 (2011).

[10] D. Li, *Electrokinetics in Microfluidcs* (Elsevier Ltd, New York, 2004).

[11] C. Rice and R. Whitehead, J. Phys. Chem. **69**, 4017 (1965).

[12] G. M. Mala, D. Li, C. Werner, and H. Jacobasch, Int. J. Heat Fluid Flow **18**, 489 (1997).

[13] Y. Gao, T. N. Wong, C. Yang, and K. T. Ooi, J. Colloid Interface Sci. **284**, 306 (2005).

[14] H. Aref, J. R. Blake, M. Budišić, J. H. E. Cartwright, H. J. H. Clercx, U. Feudel, R. Golestanian, E. Gouillart, Y. Le Guer, G. F. van Heijst, T. S. Krasnopolskaya, R. S. MacKay, V. V. Meleshko, G. Metcalfe, I. Mezić, A. P. S. de Moura, K. El Omari, O. Piro, M. F. M. Speetjens, R. Sturman, J.-L. Thiffeault, and I. Tuval, Rev. Mod. Phys. **89**, 025007 (2017).

[15] H. Aref, Phys. Fluids **14**, 1315 (2002).
[16] A. Ajdari, Phys. Rev. Lett. **75**, 755 (1995).
[17] A. S. W. Ng, W. L. W. Hau, Y. Lee, and Y. Zohar, J. Micromech. Microeng. **14**, 247 (2004).
[18] A. K. De, A. Mukhopadhyay, and I. K. Puri, Microfluid. Nanofluid. **4**, 463 (2008).
[19] R. Chabreyrie, C. Chandre, and N. Aubry, Phys. Fluids **23**, 072002 (2011).
[20] S. S. W. S. Jones, O. O. M. Thomas, H. Aref, and O. O. M. Thomas, J. Fluid Mech. **209**, 335 (1989).
[21] P. Garg, J. R. Picardo, and S. Pushpavanam, Phys. Fluids **27**, 032004 (2015).
[22] J. R. Pacheco, K. Ping Chen, and M. A. Hayes, Fluid Dyn. Res. **38**, 503 (2006).
[23] S. J. Kim, I. S. Kang, and B. J. Yoon, Chem. Eng. Commun. **193**, 1075 (2006).
[24] N. S. Lynn, C. S. Henry, and D. S. Dandy, Microfluid. Nanofluid. **5**, 493 (2008).
[25] T. Krishnaveni, T. Renganathan, and S. Pushpavanam, Ind. Eng. Chem. Res. **56**, 4145 (2017).
[26] D. Di Carlo, Lab Chip **9**, 3038 (2009).
[27] S. Wiggins and J. M. Ottino, Philos. Trans. A. Math. Phys. Eng. Sci. **362**, 937 (2004).
[28] M. Camesasca, M. Kaufman, and I. Manas-Zloczower, Macromol. Theory Simul. **15**, 595 (2006).
[29] H. Holden, K. H. Karlsen, K.-A. Lie, and N. H. Risebro, *Splitting Methods for Partial Differential Equations with Rough Solutions* (European Mathematical Society, Switzerland, 2010).
[30] Y. Wang and K. Hutter, Int. J. Numer. Methods Fluids **37**, 721 (2001).
[31] S. F. Davis, SIAM J. Sci. Stat. Comput. **8**, 1 (1987).
[32] H. J. Kim and A. Beskok, J. Micromech. Microeng. **17**, 2197 (2007).
[33] J. P. Gleeson, Phys. Fluids **17**, 100614 (2005).
[34] M. Gao and L. Gui, J. Micromech. Microeng. **26**, 075005 (2016).